

Finite element analysis of a personalized femoral scaffold with designed microarchitecture

P Pandithevan¹ and G Saravana Kumar^{2*}

¹Department of Mechanical Engineering, Indian Institute of Technology Guwahati, Guwahati, India

²Department of Engineering Design, Indian Institute of Technology Madras, Chennai, India

The manuscript was received on 9 April 2009 and was accepted after revision for publication on 28 October 2009.

DOI: 10.1243/09544119JEIM633

Abstract: Tissue engineering scaffolds with intricate and controlled internal structure can be realized using computer-aided design (CAD) and layer manufacturing (LM) techniques. Design and manufacturing of scaffolds for load-bearing bone sites should consider appropriate biocompatible materials with interconnected porosity, surface properties, and sufficient mechanical properties that match the surrounding bone, in order to provide adequate support, and to mimic the physiological stress–strain state so as to stimulate new tissue growth. The authors have previously published methods for estimating subject- and site-specific bone modulus using computed tomography (CT) data, CAD, and process planning for LM of controlled porous scaffolds. This study evaluates the mechanical performance of the designed porous hydroxyapite scaffolds in load-bearing sites using a finite element (FE) approach. A subject-specific FE analysis using femoral, defect site geometry and anisotropic material assignment based on CT data is employed. Mechanical behaviour of the femur with scaffold in stance-phase gait loading, which has been shown experimentally to produce clinically relevant results, is analysed. The comparison of results with simulation of healthy femur shows an overall correspondence in stress and strain state which will provide optimized mechanical properties for avoiding stress shielding, and adequate strength to avoid failure risk and for active bone tissue regeneration.

Keywords: femoral scaffold, biomimetic design, layered manufacturing, mechanical properties, finite element analysis

1 INTRODUCTION

Repairing bone defects resulting from tumour removal, large segmental fracture, etc. requires grafts; tissue engineering has shown great promise in the culture of tissue both *in vitro* and *in vivo*. The bone tissue engineering uses scaffolds that fill the defect, stimulate new bone tissue growth, and become resorbed over time as they are replaced by newly formed bone. The scaffold's internal architecture plays an essential role, in particular the porosity, pore size, and pore interconnectivity that provide a suitable biological environment for cell proliferation, tissue regeneration, and nutrient flow

[1–6]. Furthermore, in the case of a scaffold material with high bulk modulus, the relatively low elastic modulus of porous scaffold material can reduce the extent of stress shielding, which causes bone resorption. The scaffold should bear the load imposed during the early recovery period without collapsing and the stiffness of the scaffold should be equal to or slightly less than the surrounding bone, so that stress shielding is avoided [7–9]. Many natural biomaterials (e.g. collagen and chitin) and synthetic biomaterials (e.g. poly(a-hydroxyesters) and poly(anhydrides) [10, 11], hydroxyapite (HA) [12, 13], tricalcium phosphate (TCP) ceramics [14, 15], polycaprolactone (PCL) [16], and metal such as titanium [17]) have been widely and successfully used as scaffolding materials because of their good cell–tissue biocompatibility and processability. The complexity of architecture and the variability of

*Corresponding author: Engineering Design, Indian Institute of Technology, Madras, Chennai, Tamilnadu 600036, India.
email: gsaravana@iitm.ac.in

properties of bone tissue (e.g. porosity, pore size, mechanical properties, mineralization or mineral density, and cell type), as well as differences in age, nutritional state, activity (mechanical loading), and disease status of individuals establish a major challenge in fabricating scaffolds and engineering bone tissues that will meet the needs of specific repair sites in specific patients.

The conventional scaffold fabrication techniques produce process-dependent architectures that are incapable of precisely controlling pore size and shape, porosity, and their spatial distributions within the scaffold volume [18, 19]. The advent of layer manufacturing (LM) technologies has overcome many limitations related to both the design and the fabrication of tissue engineering scaffolds [20, 21]. In particular, these technologies allow the fabrication of scaffolds with customized global anatomical shape, via combination with reverse engineered data from computed tomography (CT) or magnetic resonance imaging [22], with virtually no limits on the complexity of the geometry achievable. In addition, reproducible and irregular internal structures can be obtained, giving control over pore size, shape, interconnectivity, and porosity [23, 24]. The design of the global and internal architectures of scaffolds can be performed and precisely controlled within three-dimensional (3D) computer-aided design (CAD), a characteristic that may improve the flow of essential nutrients across the scaffold geometry, thereby aiding a deeper regeneration of new tissue [2, 4, 25–28]. A commonly used approach is to design the external geometry and the internal architecture as special interconnected channels using CAD based cellular models, and the two geometric models are merged using Boolean operation [24]. This approach presents several drawbacks, such as limited gradients of pore size and shape, porosity, and lack of irregularities, unlike the features observed in natural trabecular bone structure [29]. In addition, the need for CAD Boolean operations makes the process particularly inefficient when the geometries to be merged become very complex and irregular, as in such cases the amount of computational time, resources, and file size increase enormously. As a result, the scaffold architectures are often limited to regular primitive shapes in the form of patterned straight lines, or square or circular holes [30].

The present study considers bone tissue engineered scaffolds with controlled internal architecture for generic femoral bone defect sites. The Young's modulus of cortical bone is reported to lie

in the range of 5–21 GPa and that of trabecular bone is reported to be less than 5 GPa. The external geometry and the distribution of bone material in space continuously adapts to the prevailing physiological loading conditions [31]. The internal structural design of scaffold should consider this site-specific regional variation of stiffness so as effectively to avoid stress shielding [9]. The variation of bone stiffness is predominantly attributed to the variation of cortical bone properties rather than that of trabecular bone [32, 33]; also, cortical bone strength is better correlated with cortical porosity rather than bone mineral density [34]. Considering these aspects, the current authors have earlier proposed a subject-specific 3D reconstruction protocol that models cortical porous geometry and thereby the site-specific modulus requirement apart from external geometry for the scaffold design [35]. The literature reports methods for creating porous geometry using LM, although these methods either require special geometric data to be modelled in CAD [36] or there is no local control in heterogeneity of porosity [37]. In a LM process the porosity of the deposited volume can be controlled by certain parameters, namely, the layer thickness t , the raster pattern, and the road width of the raster path w . The road width w depends on the LM system hardware, e.g. in the case of fused deposition modelling it depends on the diameter of polymer extruder nozzle. To vary the volume fraction or porosity of material being deposited in a unit area and thereby to control the porosity, location-controlled density raster tool paths using fractal curves have been proposed previously by the current authors [38]. With these techniques, the authors have proposed a methodology to biomimetic design and process planning for LM of patient- and site-specific porous scaffolds so as to match the mechanical properties of scaffold to the surrounding bone defect site [39]. In that study of correlation models between porosity and modulus for bone, known biomaterials processable by LM such as HA, PCL, TCP, and titanium were used to estimate the site-specific porosity requirements in the scaffold model. The various constraints due to pore size requirement for repair and regeneration of bone, available choice of LM tool path width, and limited choice of LM-processable materials resulted in some mechanical stiffness mismatch between the bone site requirement and the designed scaffold. This paper reports the results of prediction of mechanical response of the human femur with such bone replacement to a physiological loading condition. Subject-specific finite element (FE) models of

bones derived from CT data are a promising tool to assess non-invasively the stress state and fracture risk of bones, as well as the design and the optimization of prosthetic and replacement devices [40, 41]. Three-dimensional FE analyses of healthy bone and bone with defect sites replaced by designed HA scaffold are used to understand the mechanical response for assessing the scaffold design subject to constraints in LM.

2 METHODOLOGY

Figure 1 schematically illustrates the complete methodology for biomimetic design and LM for subject-

and site-specific femoral bone scaffolds with controlled internal architecture that match surrounding bone properties. The complete methodology can be grouped into three phases. The initial phase consists of subject-specific 3D reconstruction of femur bone. Subsequently, in the second phase, a CAD model of the scaffold with site-specific porosity is derived from the reconstructed femoral bone model. A novel tool path generation method for LM using space-filling fractal curves is later employed in phase three for downstream LM of the scaffold. The details of these methodologies are described in previous publications by the present authors and only salient points will be discussed here to aid understanding. A representative case

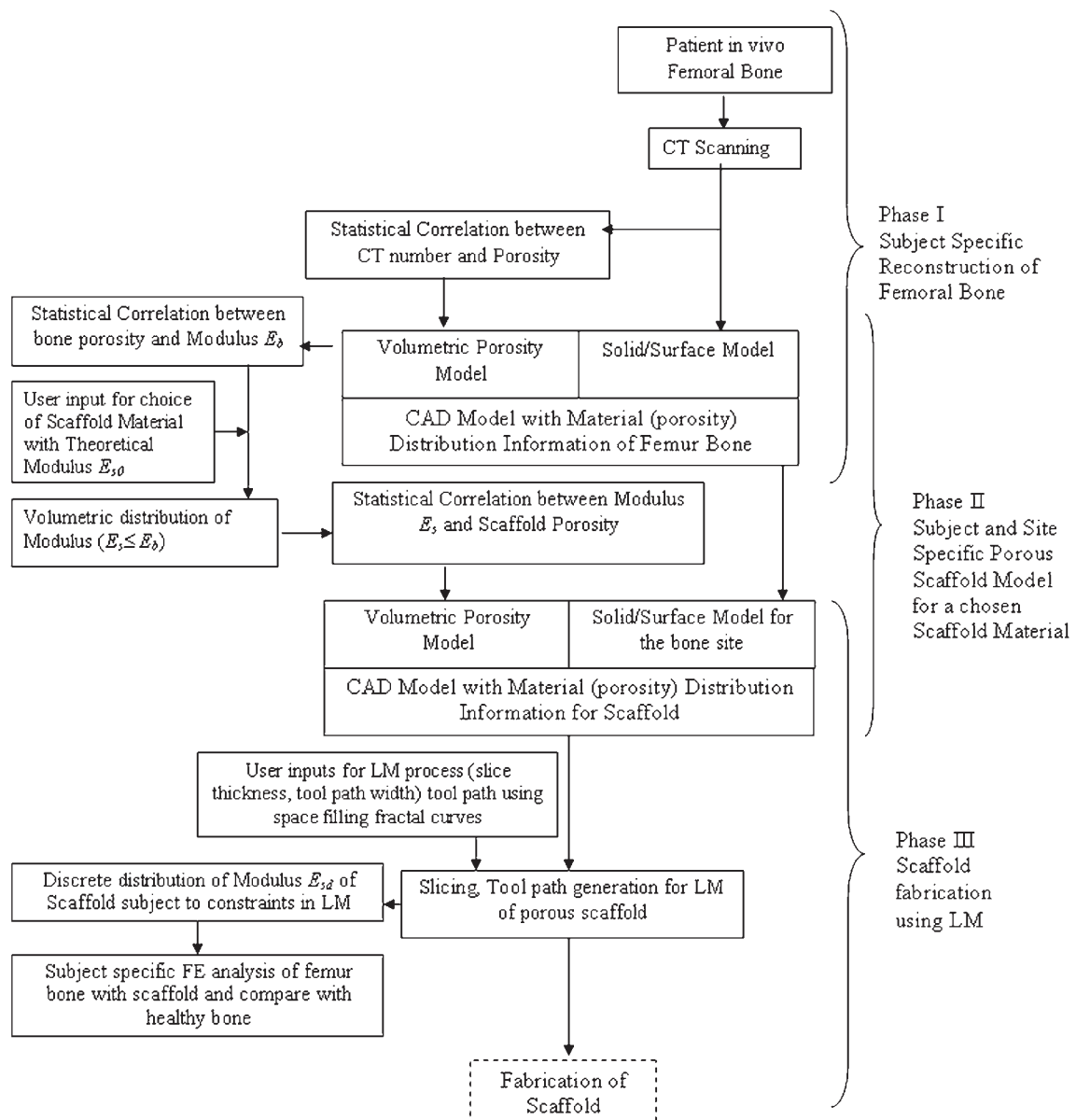


Fig. 1 Schematic diagram of the proposed methodology

study considering HA scaffold design and process planning in LM for a human femur defect site has also been presented to illustrate the methodology by the authors [39]. A 3D finite element analysis (FEA) of healthy bone and bone with the defect site replaced using the designed scaffold was envisaged to understand the mechanical response for assessing and optimizing the scaffold design subject to constraints in LM.

2.1 Subject-specific reconstruction of femoral bone along with internal properties

As the mechanical properties of femoral bone vary with the individual and with the location for an individual [42], the proposed method aims to control the scaffold properties in a subject- and site-specific way. The present work requires an estimation of porosity by using the CT number of a commercially available medical scanner, so a 3D reconstruction methodology proposed by the authors [35] is used. The subject-specific external geometry from a CT image is obtained using the commercial software Mimics®. Using the correlation models (equations (1) and (2)) developed in reference [35], voxel data of mean porosity or apparent density are computed depending on the CT value range, and along with the reconstructed surface model form the subject-specific CAD model of the femur, with material density (porosity) as shown in Fig. 2. Site-specific porosity/apparent density data can now be extracted

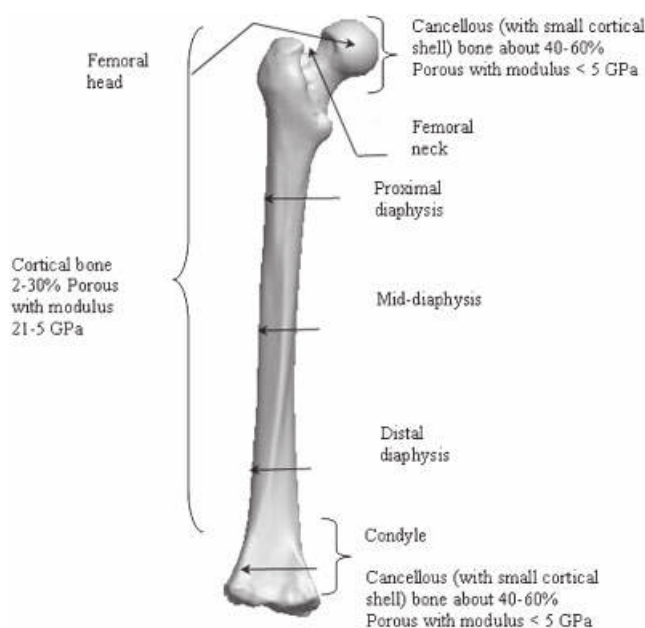


Fig. 2 Human femur anatomy with porosity and stiffness at different region [35]

from this model so as to design scaffolds that match the surrounding healthy bone modulus.

$$p_c = -0.0362HU + 59.96 \text{ (per cent)},$$

$$R^2 = 0.94 \quad \text{and} \quad P(t) < 0.05$$

$$800 \leq HU \leq 1800$$
(1)

$$\rho_t = \frac{2}{1800} HU \text{ (g/cm}^3\text{)}, \quad HU < 800$$
(2)

2.2 Subject- and site-specific porous scaffold model

The scaffold is modelled with two components: the external geometry and the internal architecture as depicted schematically in phase two of the overall methodology (Fig. 1). The external geometry of the scaffold must have a good fit inside the defect and thus the shape of scaffold is extracted from clinical CT images of the bone defect using Mimics. The internal architecture of the scaffold should be modelled such that Young's modulus of the scaffold is the same or slightly less than the modulus of the surrounding bone. The internal architecture is not modelled as an extra cellular matrix and Booleaned with the external geometry, as has been done by other researchers [7, 36]. A methodology proposed by the present authors [38, 39] is used where the internal architecture property is modelled as a mathematical volumetric model containing the mechanical modulus and porosity information corresponding to the bone defect. A three-step correlation is used to obtain these volumetric data. First the CT number to bone site porosity or apparent density is determined using equations (1) and (2), and then the bone modulus is determined using relations developed by Dong and Guo [43] and Rho *et al.* [44], for cortical and trabecular bone respectively (equations (3) and (4)).

$$E_c = -0.53 \left(\frac{P_c}{100} \right) + 21.43 \text{ (GPa)} \quad (R^2 = 0.66)$$
(3)

$$E_t = 4.607(\rho_t)^{1.30} \text{ (GPa)} \quad (R^2 = 0.6)$$
(4)

Finally, empirical relations and correlation that describe the Young's modulus and porosity correlation for HA [13], which is a LM processable biomaterial, as given in equation (5), are used to

estimate the required scaffold porosity. The correlation derived between CT number of a bone site and the required HA scaffold porosity is given in equation (6) so that the stiffness is compatible.

$$E_{\text{HA}} = 140 e^{-3.68 (p/100)} \quad (\text{GPa}) \quad (5)$$

$$p_{\text{HA}} = \frac{\log[(0.019186\text{HU} - 10.3488)/140]}{-3.68} \times 100 \quad (\text{per cent}) \quad (6)$$

2.3 Process planning for LM of a scaffold

In the proposed framework and methodology (Fig. 1), the solid model (S) of a porous scaffold contains two types of information; geometrical model of the scaffold (G) and material porosity model for the scaffold (M). The overall process of converting the solid model S to tool path specification for LM is done separately for the geometric model G and the material porosity model M , and finally the information is merged to give the tool path. Slicing is the first step in part building by any LM process. The 3D solid model has to be converted into a series of two-dimensional (2D) slices (contours representing boundaries) depending on the slice thickness t specified by the user. The information processing for the geometric model G is carried out using the front end software of the LM machine to give a series of 2D contours (GC_i , $i = 1, 2, \dots, n$). The procedures for information processing for the material porosity model M have been developed in the current authors' earlier work and algorithms implemented in a Matlab® programming environment [38]. The material porosity model M is sliced such that it yields 2D material porosity contours (MC_i , $i = 1, 2, \dots, n$). A slice of the material porosity model specifies the material porosity variation for the corresponding slice from geometry, i.e. for an i th slice, GC_i specifies the boundaries and MC_i specifies the material porosity variations. The tool path for LM consists of the boundary contour and the raster tool paths (for filling). In the present work the authors have used a novel method proposed earlier [38] for generating boundary-constrained controlled-density raster tool paths from the porosity model M using continuous space filling fractal curves. Figure 3 illustrates the fractal tool paths for graded porous objects using an example slice consisting of an arbitrary geometric boundary GC_i and a material porosity contour MC_i that specifies progressively

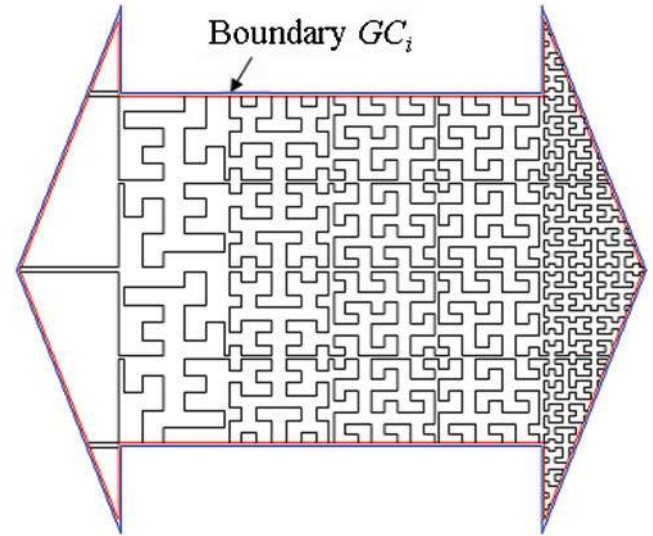


Fig. 3 Fractal tool paths in LM of graded porous objects. The figure illustrates a material slice MC_i that progressively becomes denser towards the right, trimmed by an arbitrary geometric boundary GC_i

increasing density towards the right. It can be noticed that as the density increases, the type of fractal curve changes, as well as its level of decomposition, increases. In the proposed scheme, in order to obtain a particular volume fraction or material porosity in the scaffold as specified by the porosity contours MC_i , it is necessary to choose the appropriate type of fractal curve and its level of decomposition for a fixed road width w , considering the area filling characteristics and slice thickness t . The procedure of generating boundary-constrained raster tool paths takes care of the intersection operator on G and M . The results of modelling the scaffold for a defect region, obtaining boundary-constrained controlled-density raster tool paths in LM is described in Fig. 4.

2.4 Mechanical evaluation

The mechanical response of the human femur with such bone replacement to loading condition is assessed using the finite element method (FEM) and compared with healthy femur. The generation of the FE models from the CT data-set is similar to the method described in detail by Taddei *et al.* [40]. CT data-sets were segmented using Mimics and surface mesh models were exported to Abaqus®, where tetrahedral elements were created for FEA. Inhomogeneous material properties were automatically mapped on to the FE models with the BoneMat software [40, 45] that calculates an average Young's

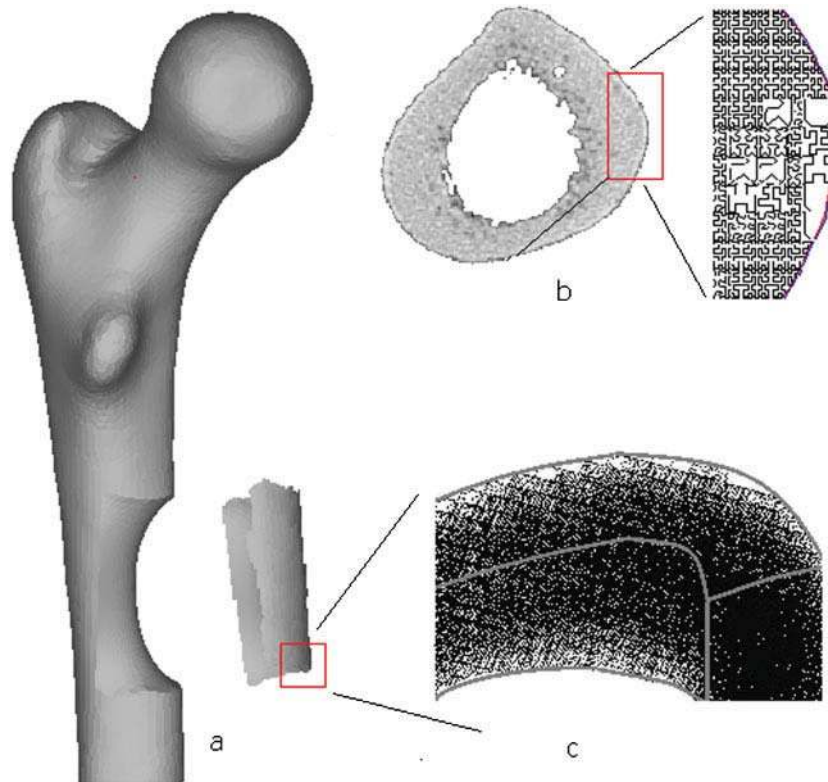


Fig. 4 External geometry and internal architecture of the scaffold using the biomimetic design and LM using fractal geometry [39]: (a) bone defect site and external geometry of scaffold; (b) one representative CT slice with marked defect site and the reconstructed scaffold layer; (c) 3D stack of layers of fractal curves

modulus (E) for each element of the mesh corresponding to the HU value from the CT data. Mesh convergence studies [41, 46] are important to obtain converged stiffness, stress, and risk results. A mesh convergence study was performed on the femur data with element edge lengths of 4.5, 3, and 1.5 mm. To validate the procedure and compare the results of the convergence study, the material assignment based on apparent density ($\rho_{app} = 1 + 7.185 \times 10^4$ HU in g/cm^3) and power law relations between modulus and density ($E_b = 1.99 \times 10^3 \rho^{3.46}$ in GPa) [47] and boundary conditions as reported by Laz *et al.* [41] were utilized. The validation and convergence of mesh size is based on the maximum von Mises stress. Maximum von Mises stress was computed for each trial, while excluding the distal end of the femur, owing to discontinuities associated with the fixed boundary condition. The results for the 3 mm and 1.5 mm element meshes exhibited convergence with details provided in the results section.

The two models, i.e. femur model with bone properties and femur model with scaffold replacement using appropriate scaffold material property,

were subjected to simulation of similar loading conditions. The material assignment for bone is conducted by converting the CT numbers to Young's modulus by using equations (1) and (3) for the cortical region and equations (2) and (4) for the trabecular region as shown in Fig. 5(a). For the femur with scaffold replacement, the region of scaffold replacement is assigned Young's modulus using equation (5) for the HA scaffold material. The porosity requirement as per equation (6) is computed and only the discrete value is assigned owing to constraints in the available range of LM tool path width. Both materials bone and HA were modelled as isotropic and a Poisson ratio of 0.3 was assumed [48]. In the normal range of regular daily activities, the bone exhibits elastic linear behaviour for loads [49] and this assumption is used for the analysis. The influence of strain rate was considered negligible as the tests were conducted in quasi-static conditions. The boundary condition for simulation is based on stance-phase gait loading, which has been shown experimentally to produce clinically relevant results [50–52]. The study considered a loading configuration frequently used in the literature in order to

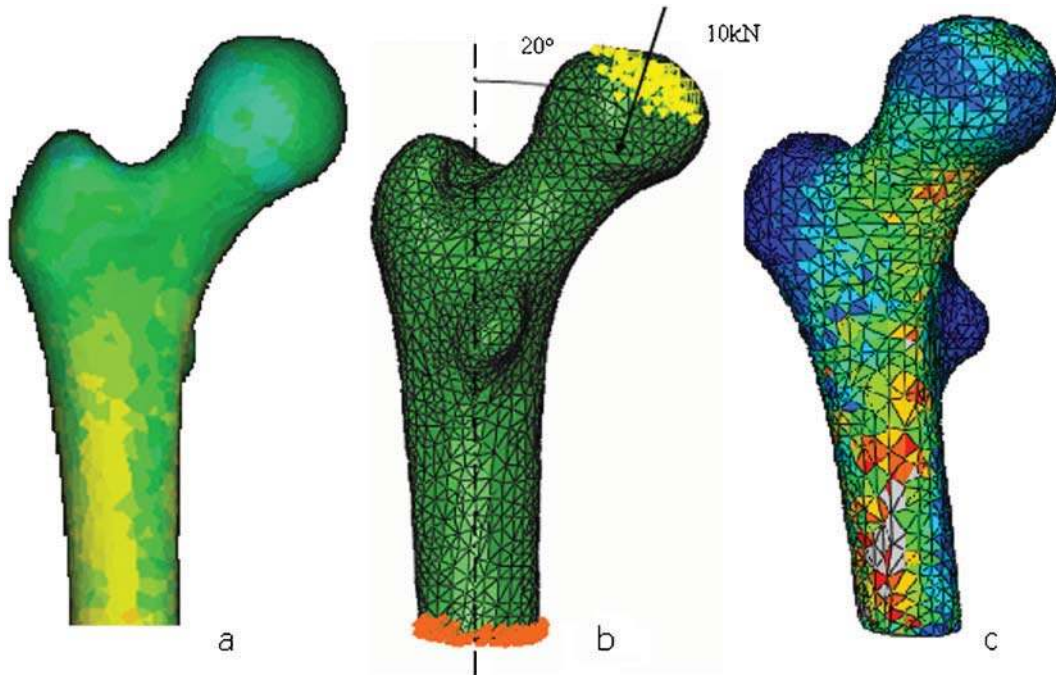


Fig. 5 Finite element model of femur bone: (a) distribution of modulus; (b) loading condition; (c) stress contours

replicate simplified single-leg stance. The femur was simulated with the hip joint resultant force assumed to be in the plane of the femoral diaphysis. The distal end of each femur was fixed, while a load of 10 kN was applied to the femoral head at an angle of 20° to the shaft axis in the frontal plane, as shown in Fig. 5(b). The centre of rotation for the angle is the intersection of the femoral shaft axis, which passed through the centre of the proximal portion of the femoral shaft, and the loading axis, which passed through the centre of the femoral head. The applied load of 10 kN was based on the 75 per cent load of experimentally measured fracture load under stance conditions [50]. The load was distributed evenly among nodes on the femoral head that were located within 1.5 cm from the centre of load application [51].

The analysis was performed and the mechanical behaviour of healthy femur and femur with scaffold replacement were compared. For evaluation of the biomimetic ability of the scaffold, the following parameters were computed. First, the mismatch between the required stiffness and the stiffness assigned for the elements corresponding to the defect site were analysed. As failure of a single element may be attributed to an artifact due to meshing and or CT data and need not constitute structural failure, the histograms of von Mises stress over all the elements in the model are computed. If

the femur bone and femur bone with scaffold have comparable histograms, one can expect that they will fail in a similar way. Finally, a histogram of the magnitude of the highest principal strains (compression or tension) over all the elements in the model was computed. This is a measure of activation of osteoblasts growing in the scaffold. If the scaffold and the bone have a comparable histogram, one can expect the osteoblasts in the scaffold to be activated in the same way as if they were inside real bone [7, 53].

3 RESULTS AND DISCUSSION

The present study assesses the designs of subject- and site-specific porous scaffold that have matched external geometry, biological, and mechanical behaviour to the femoral bone defect site using FEA. A healthy human right femur was CT scanned and an imaginary femoral defect is considered to illustrate the methodology and study the results. The defect area is to be replaced by a biomimetic scaffold made of HA. A sample defect area with a gross volume ($30\text{ mm} \times 6\text{ mm} \times 20\text{ mm}$) was chosen near the medial mid-diaphysis. The femur was CT scanned as per the established protocol. Mimics was used to reconstruct the external geometry of the femur and the external geometry of an artificial model of the

imaginary defect area, as shown in Fig. 4(a). After segmentation of the defect area, the corresponding voxels were processed and material porosity model (M) of the HA scaffold determined. The voxel resolution for the scan was $0.20\text{ mm} \times 0.20\text{ mm} \times 0.60\text{ mm}$. For reconstructing the internal architecture, a resampling of this voxel set at a resolution of $1\text{ mm} \times 1\text{ mm} \times 1.2\text{ mm}$ was carried out to reduce the computational load and a voxel set of ~ 2850 voxels corresponding to the defect area was processed by using procedures described in the present authors' earlier work [39]. One representative slice is shown in Fig. 4(b) that describes the process planning in LM (slicing, fractal raster tool path in LM). A small region of the model of the scaffold showing layers of such fractal curves is shown in Fig. 4(c).

In the present case study the defect site chosen in the femur has stiffness in the range of 10–18 GPa. The theoretical stiffness of the dense HA is 140 GPa, which is much higher than that of human bone, which requires stiffness in the range close to ~ 20 GPa. In order to match the stiffness site-specifically, the correlation models predict a required porosity in the range 70–50 per cent to be assigned to the various voxels. Using the equations developed in earlier work [39] that predict the area filling characteristic of fractal curves (12 designs are

considered in total), appropriate combinations of fractal space-filling curves were selected and combined to generate the fractal tool path for a tool path width $w = 0.06\text{ mm}$ and slice thickness $t = 0.0625\text{ mm}$ (commercially available in stereolithography apparatus for processing HA). Only three designs had the area-filling characteristics for the range of porosity required (i.e. 50–70 per cent). This resulted in a discrete set of porosity values, namely 55.08 per cent, 61.46 per cent, and 71.44 per cent, to be assigned to the various voxels corresponding to the scaffold volume. This limitation is due to the tool path designs considered in the study [39] and is not process-specific; it can be overcome in future by considering more tool paths for microarchitecture design. Figure 6 shows the possible discrete percentage porosity in the HA scaffold material. The corresponding stiffnesses allocated to the various voxels considered for the defect site were 18.44 GPa, 14.58 GPa, and 10.10 GPa. This allocation led to some mismatch in stiffness required and the stiffness allocated, and the same is qualified statistically. The stiffness assignments for ~ 2850 voxels corresponding to the defect site were analysed with cumulative frequency of stiffness mismatch in intervals of 0.25 GPa (Fig. 7). The histograms show that the stiffness of HA scaffold is matched closely to

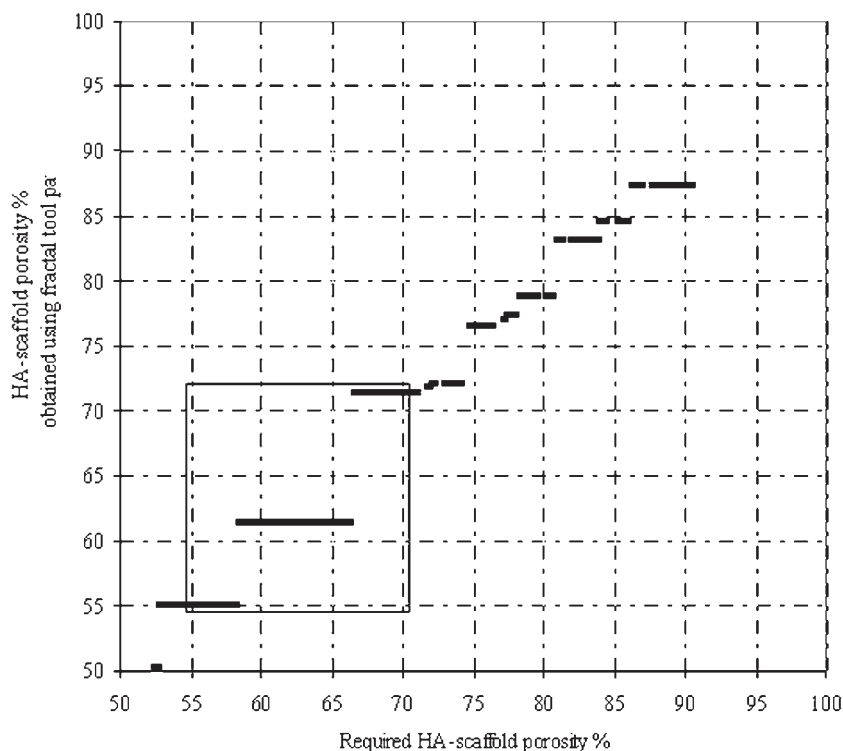


Fig. 6 Estimated porosity (to match bone stiffness) and obtained porosity in HA in LM for a tool path width $w = 0.06\text{ mm}$ and slice thickness $t = 0.0625\text{ mm}$ [39]

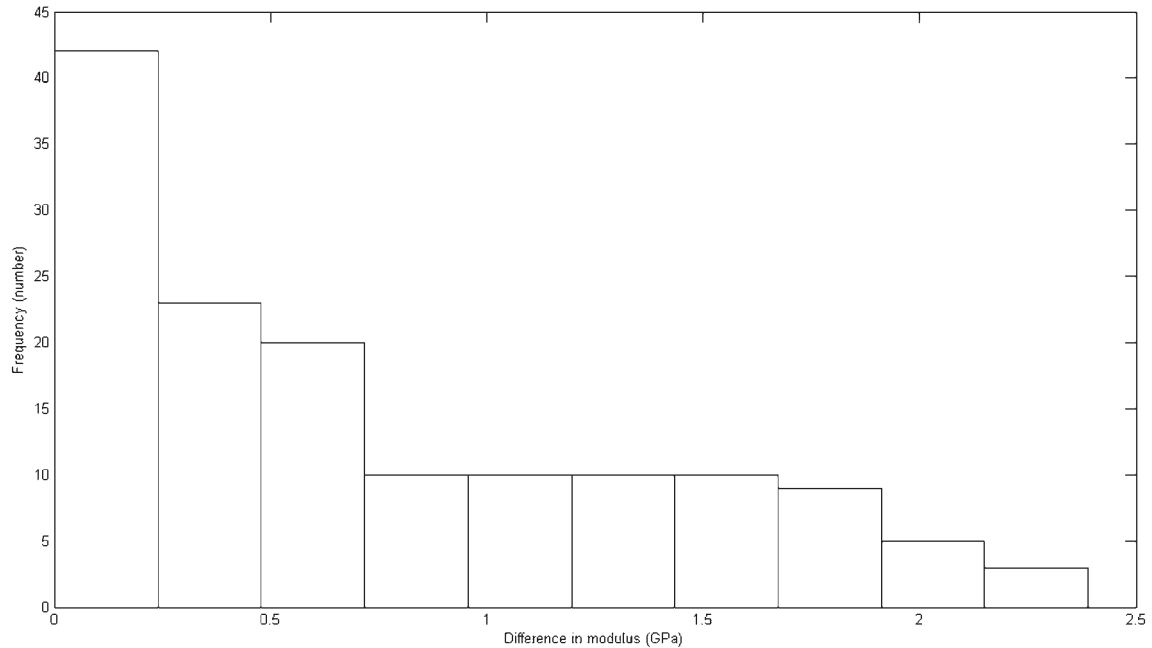


Fig. 7 Cumulative frequency of stiffness mismatch between bone and HA scaffold

the corresponding stiffness of the femur defect site, with maximum frequency of mismatch corresponding to stiffness difference of less than 1 GPa.

The biomimetic ability of the HA scaffold was evaluated using FE simulation. The model predicted the stress and strain for every element in a healthy femur as well as femur with scaffold replacement (Fig. 5(c)). To validate the procedure, an analysis was performed on the femur geometry with the material assignment and boundary conditions the same as reported by Laz *et al.* [41]. Stresses were highest in the femoral neck region. The maximum von Mises stress was found to be 112 MPa, which lies in the range 110–150 MPa as reported in reference [41] from the simulations on five femurs. The results of the mesh convergence study (Fig. 8) exhibited convergence for the 3 mm mesh with differences less than 2 per cent for maximum von Mises stress values when compared with the 1.5 mm mesh. Results presented for the femur and femur with scaffold were based on the 3 mm results. On both models, the material assignment for the bone region was conducted as described by equations developed in the present work (section 2.2) and for the defect region with scaffold using discrete values of stiffness subject to constraints in LM; simulation was carried out as per the boundary conditions reported by Laz *et al.* [41].

The maximum von Mises stress in the neck region (Fig. 5(c)) is 81 MPa and 88 MPa for femur bone and bone with scaffold respectively. Figure 9 shows the computed histograms of the von Mises stress on all

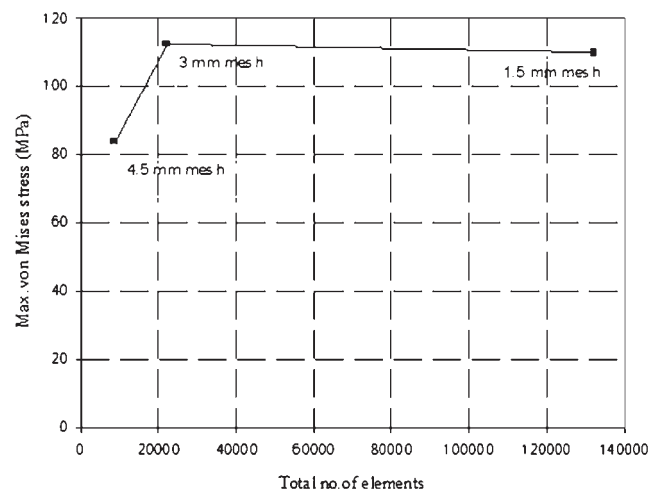


Fig. 8 Mesh convergence study for three different mesh sizes

elements in the femur bone model, and the femur bone model with HA scaffold. The comparison of stress histograms predominantly shows a good correspondence between the bone and bone with HA scaffold model, thus the risk of failure may be expected to be the same. When subjecting the scaffold to physiological load, the strain distribution should be such that the majority of the osteoblasts should feel a strain that activates them. This happens for strains in the range 1000–4000 $\mu\epsilon$ [7, 53]. The strain histograms were computed for this range of maximum principal strain on all elements

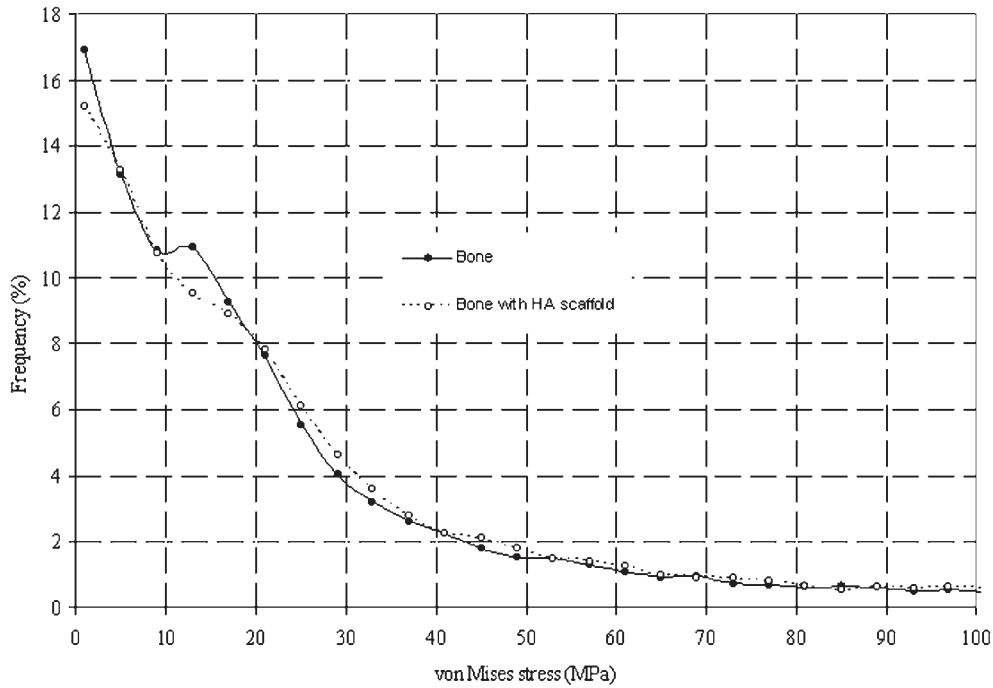


Fig. 9 Histograms of von Mises stress in bone and bone with HA scaffold

in the femur bone model and the femur bone model with HA scaffold, as shown in Fig. 10. The comparison of strain histograms shows an overall correspondence. The number of elements having strain in the range 1000–4000 $\mu\epsilon$ is slightly fewer in the femur with HA scaffolding in the defect site, when compared with healthy femur.

The FEA shows that there is some stiffness mismatch between the assignment and that required for the HA scaffold. This has led to differences in the stress histogram, particularly in the stress range 10–20 MPa (Fig. 9), and differences in strain. The results of FEA confirm the biomimetic ability of the designed personalized scaffold. The mechanical properties are

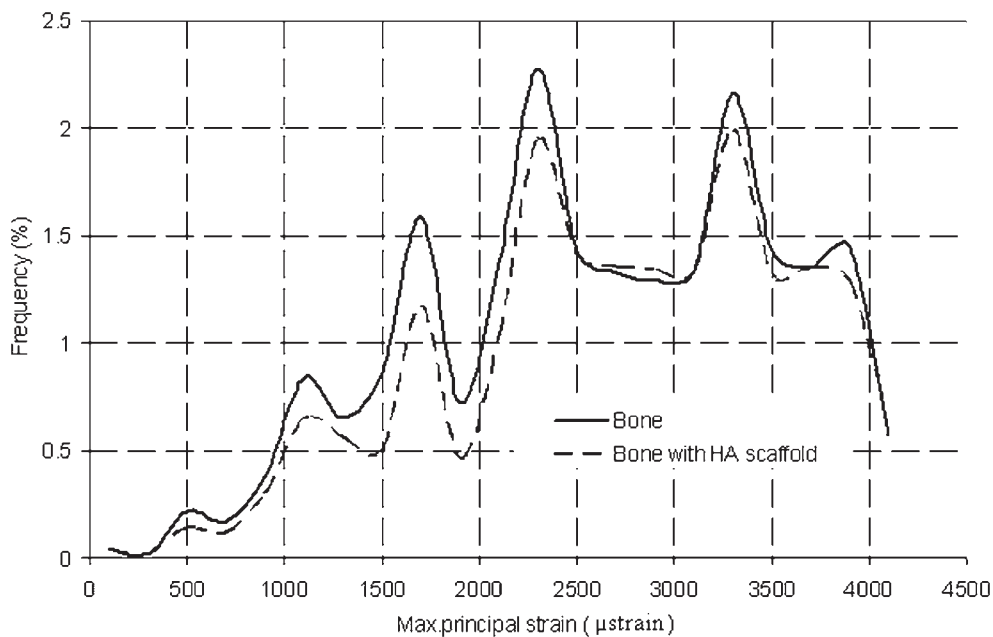


Fig. 10 Histograms of principal strain in bone and bone with HA scaffold

closely matched to those of the healthy bone for load bearing as well as for a good stimulation for new bone tissue growth through activation of osteoblasts. In the current study, only the mechanical and anatomical factors have been considered for the biomimetic design. In this work, the von Mises stress and maximum principal strain were considered for evaluation. The advantages of using other criteria can be explored. The differences in the stress and strain state between the healthy femur and femur with scaffold can be reduced by exploring HA blends with other biocompatible materials such as TCP ceramics, which have better resorbability and lower bulk modulus. The simulation predicted the behaviour of the femur with designed scaffold for during clinically significant stance-phase gait loading and early recovery period. In future, the present authors intend to study the behaviour of the femur with the designed scaffold for other loading conditions and for different periods of bone regeneration in the scaffold. Future studies will also be aimed at physical realization of the designed scaffolds in LM hardware and comprehensive assessment of tissue growth considering biological, anatomical, and mechanical factors.

4 CONCLUSIONS

In summary, the proposed methodology of biomimetic design using reconstruction based on a commercial low-resolution CT scanner and LM of a controlled porous structure using fractal tool paths has proven to represent correctly the internal architecture patterns, apart from external geometry, for subject- and site-specific femoral bone scaffolds. The present approach leads to controlled porous architecture with porosity and stiffness that are important for vascularization and resorption. The example case study illustrated the complete methodology for designing a scaffold for a defect site using HA biomaterial. The spectrum of stiffness assignment in the scaffold is limited by the fractal patterns and tool path widths available in LM machines that can process the scaffold material. The detailed FEA involving subject-specific femoral geometry, defect site, and anisotropic material assignment predicted the effect of the stiffness mismatch, allowing for design validation of a scaffold with mechanical properties to avoid stress shielding, with adequate strength to avoid risk of failure, and for active bone tissue regeneration.

© Authors 2010

REFERENCES

- 1 Vuola, J., Taurio, R., Göransson, H., and Askö-Seljavaara, S. Compressive strength of calcium carbonate and hydroxyapatite implants after bone-marrow-induced osteogenesis. *Biomater.*, 1998, **19**, 223–227.
- 2 Chu, T. M. G., Orton, D. G., Hollister, S. J., Feinberg, S. E., and Halloran, J. W. Mechanical and *in vivo* performance of hydroxyapatite implants with controlled architectures. *Biomater.*, 2002, **23**, 1283–1293.
- 3 Taboas, J. M., Maddox, R. D., Krebsbach, P. H., and Hollister, S. J. Indirect solid free form fabrication of local and global porous, biomimetic and composite 3D polymer-ceramic scaffolds. *Biomater.*, 2003, **24**, 181–194.
- 4 Sun, W., Starly, B., Darling, A., and Gomez, C. Computer aided tissue engineering: application to biomimetic modeling and design of tissue scaffold. *Biotechnol. Appl. Biochemistry*, 2004, **39**(1), 49–58.
- 5 Yang, S., Leong, K. F., Du, Z., and Chua, C. K. The design of scaffolds for use in tissue engineering. Part 1: traditional factors. *Tissue Engng*, 2001, **7**(6), 679–689.
- 6 Yang, S., Leong, K. F., Du, Z., and Chua, C. K. The design of scaffolds for use in tissue engineering. Part 2: rapid prototyping techniques. *Tissue Engng*, 2002, **8**(1), 1–11.
- 7 Cleynenbreugel, T. V., Oosterwyck, H. V., Sloten, J. V., and Scrooten, J. Trabecular bone scaffolding using biomimetic approach. *J. Mater. Sci.: Mater. in Medicine*, 2002, **13**, 1245–1249.
- 8 Woesz, A., Stampfl, J., and Fratzl, P. Cellular solids beyond the apparent density – an experimental assessment of mechanical properties. *Advd Engng Mater.*, 2004, **6**(3), 134–138.
- 9 Leong, K. F., Chua, C. K., Sudarmadji, N., and Yeong, W. Y. Engineering functionally graded tissue engineering scaffolds. *J. Mech. Behavior Biomed. Mater.*, 2008, **1**(2), 140–152.
- 10 Cima, L. G., Langer, R., and Vacanti, J. P. Polymers for tissue and organ culture. *J. Bioactive Compatible Polym.*, 1991, **6**, 232–240.
- 11 Zhao, F., Yin, Y., Lu, W. W., Leong, J. C., Zhang, W., Zhang, J., Zhang, M., and Yao, K. Preparation and histological evaluation of biomimetic three-dimensional hydroxyapatite/chitosan–gelatin network composite scaffolds. *Biomater.*, 2002, **23**, 3227–3234.
- 12 Lorenzo, L. M. R., Regi, M. V., Ferreira, J. M. F., Ginebra, M. P., Aparicio, C., and Planell, J. A. Hydroxyapatite ceramic bodies with tailored mechanical properties for different applications. *J. Biomater.*, 2002, **60**(1), 159–166.
- 13 He, L. H., Standard, O. C., Huang, T. T. Y., Latella, B. A., and Swain, M. V. Mechanical behaviour of porous hydroxyapatite. *Acta Biomater.*, 2008, **4**, 577–586.
- 14 Lin, L., Zhang, J., Zhao, L., Tong, A., Sun, J., and Hu, Q. Effect of microstructure on the mechanical

- properties and biology performance of bone tissue scaffolds using selective laser sintering. In Proceedings of APCMBE 2008, Beijing, China, 22–25 April 2008, *IFMBE Proceedings* (Springer, Berlin).
- 15 Lam, C. X. F., Olkowski, R., Swieszkowski, W., Tan, K. C., and Gibson, I. Mechanical and *in vitro* evaluations of composite PLDLLA/TCP scaffolds for bone engineering. *Virtual Phys. Prototyping*, 2008, **3**(4), 193–197.
 - 16 Williams, M., Adewunmi, A., Schek, R. M., Flanagan, C. L., Krebsbach, P. H., Feinberg, S. E., Hollister, S. J., and Das, S. Bone tissue engineering using polycaprolactone scaffolds fabricated via selective laser sintering. *Biomater.*, 2005, **26**, 4817–4827.
 - 17 Li, C. and Zhu, Z. Dynamic Young's modulus of open-porosity titanium measured by the electromagnetic acoustic resonance method. *J. Porous Mater.*, 2006, **13**, 21–26.
 - 18 Sachlos, E. and Czernuszka, J. T. Making tissue engineering scaffolds work. Review on the application of solid freeform fabrication technology to the production of tissue engineering scaffolds. *Eur. Cells Mater.*, 2003, **5**, 29–40.
 - 19 Tan, K. H., Chua, C. K., Leong, K. F., Naing, M. W., and Cheah, C. M. Fabrication and characterization of three-dimensional poly(ether-ether-ketone)-hydroxyapatite biocomposite scaffolds using laser sintering. *Proc. IMechE, Part H: J. Engineering in Medicine*, 2005, **219**, 183–194. DOI: 10.1243/095441105X9345.
 - 20 Yeong, W. Y., Chua, C. K., Leong, K. F., and Chandrasekaran, M. Rapid prototyping in tissue engineering: challenges and potential. *Trends in Biotechnol.*, 2004, **22**(12), 643–652.
 - 21 Yeong, W. Y., Chua, C. K., Leong, K. F., Chandrasekaran, M., and Lee, M. W. Comparison of drying methods in the fabrication of collagen scaffold via indirect rapid prototyping. *J. Biomed. Mater. Res.: Part B – Appl. Biomater.*, 2007, **82B**(1), 260–266.
 - 22 *MIMICS user manual*, 2002 (Materialise, Leuven, Belgium).
 - 23 Hutmacher, D. W. Scaffolds in tissue engineering bone and cartilage. *Biomater.*, 2000, **21**, 2529–2543.
 - 24 Sun, W., Starly, B., and Darling, A. Bio-CAD modeling and its applications in computer-aided tissue engineering. *Computer-Aided Des.*, 2005, **37**, 1097–1114.
 - 25 Bartolo, P. and Bidanda, B. *Bio-materials and prototyping applications in medicine*, 2008 (Springer-Verlag, Berlin).
 - 26 Sachlos, E., Reis, N., Ainsley, C., Derby, B., and Czernuszka, J. T. Novel collagen scaffolds with predefined internal morphology made by solid freeform fabrication. *Biomater.*, 2003, **24**, 1487–1497.
 - 27 Chua, C. K., Leong, K. F., Chua, S. W., and Cheah, C. M. Development of a tissue engineering scaffold structure library for rapid prototyping. Part 1: investigation and classification. *Int. J. Advd Mfg Technol.*, 2003, **21**, 291–301.
 - 28 Chua, C. K., Leong, K. F., Chua, S. W., and Cheah, C. M. Development of a tissue engineering scaffold structure library for rapid prototyping. Part 2: parametric library and assembly program. *Int. J. Advd Mfg Technol.*, 2003, **21**, 302–312.
 - 29 Uchiyama, T., Tanizawa, T., Muramatsu, H., Endo, N., Takahashi, H. E., and Hara, T. Three-dimensional microstructural analysis of human trabecular bone in relation to its mechanical properties. *Bone.*, 1999, **25**(4), 487–491.
 - 30 Starly, B. and Sun, W. Internal scaffold architecture designs using Lindenmayer systems. *Computer-Aided Des. Applic.*, 2007, **4**, 395–403.
 - 31 Petryl, M., Hert, J., and Fiala, P. Spatial organization of the Haversian bone in man. *J. Biomechanics*, 1991, **29**(2), 161–169.
 - 32 Schaffler, M. B. and Burr, D. B. Stiffness of compact bone: effects of porosity and density. *J. Biomechanics*, 1988, **21**(1), 13–16.
 - 33 Snyder, S. M. and Schneider, E. Estimation of mechanical properties of cortical bone by computed tomography. *J. Orthop. Res.*, 1991, **9**(3), 422–431.
 - 34 Stromsoe, K., Kok, W. L., Hoiseth, A., and Alho, A. Holding power of the 4.5 mm AO/ASIF cortex screw in cortical bone in relation to bone mineral. *Injury*, 1993, **24**(10), 656–659.
 - 35 Pandithevan, P. and Saravana Kumar, G. Reconstruction of subject specific human femoral bone model with cortical porosity data using macro-CT. *Virtual Phys. Prototyping*, 2009, **4**(3), 115–129.
 - 36 Armillotta, A. and Pelzer, R. Modeling of porous structures for rapid prototyping of tissue engineering scaffolds. *Int. J. Advd Mfg Technol.*, 2007, **39**, 501–511.
 - 37 Masood, S. H., Singh, J. P., and Morsi, Y. The design and manufacturing of porous scaffolds for tissue engineering using rapid prototyping. *Int. J. Advd Mfg Technol.*, 2005, **27**, 415–420.
 - 38 Saravana Kumar, G., Pandithevan, P., and Ambatti, A. Fractal raster tool paths for layered manufacturing of porous objects. *Virtual Phys. Prototyping*, 2009, **4**(2), 91–104.
 - 39 Pandithevan, P. and Saravana Kumar, G. Personalised bone tissue engineering scaffold with controlled architecture using fractal tool paths in layered manufacturing. *Virtual Phys. Prototyping*, 2009, **4**(3), 165–180.
 - 40 Taddei, F., Pancanti, A., and Viceconti, M. An improved method for the automatic mapping of computed tomography numbers onto finite element models. *Med. Engng Physics*, 2004, **26**(1), 61–69.
 - 41 Laz, P. J., Stowe, J. Q., Baldwin, M. A., and Petrella, A. J. Incorporating uncertainty in mechanical properties for finite element-based evaluation of bone mechanics. *J. Biomechanics*, 2007, **40**, 2831–2836.

- 42 **Cuppone, M., Seedhom, B. B., Berry, E., and Ostell, A. E.** The longitudinal Young's modulus of cortical bone in the midshaft of human femur and its correlation with CT scanning data. *Calcified Tissue Int.*, 2004, **74**, 302–309.
- 43 **Dong, X. N. and Guo, X. E.** The dependence of transversely isotropic elasticity of human femoral cortical bone on porosity. *J. Biomechanics*, 2004, **37**, 1281–1287.
- 44 **Rho, J. Y., Hobatho, M. C., and Ashman, R. B.** Relations of mechanical properties to density and CT numbers in human bone. *Med. Engng Physics*, 1995, **17**, 347–355.
- 45 **Taddei, F., Cristofolini, L., Martelli, S., Gill, H. S., and Viceconti, M.** Subject-specific finite element models of long bones: An in vitro evaluation of the overall accuracy. *J. Biomechanics*, 2006, **39**, 2457–2467.
- 46 **Perillo-Marcone, A., Alonso-Vazquez, A., and Taylor, M.** Assessment of the effect of mesh density on the material property discretisation within QCT based FE models: a practical example using the implanted proximal tibia. *Comput. Meth. Biomech. Biomed. Engng*, 2003, **6**, 17–26.
- 47 **Keller, T. S.** Predicting the compressive mechanical behavior of bone. *J. Biomechanics*, 1994, **27**, 1159–1168.
- 48 **Wirtz, D. C., Schiffers, N., Pandorf, T., Radermacher, K., Weichert, D., and Forst, R.** Critical evaluation of known bone material properties to realize anisotropic FE-simulation of the proximal femur. *J. Biomechanics*, 2000, **33**, 1325–1330.
- 49 **Keaveny, T. M., Guo, E., Wachtel, E. F., McMahon, T. A., and Hayes, W. C.** Trabecular bone exhibits fully linear elastic behavior and yields at low strains. *J. Biomechanics*, 1994, **27**, 1127–1136.
- 50 **Keyak, J. H.** Relationships between femoral fracture loads for two load configurations. *J. Biomechanics*, 2000, **33**, 499–502.
- 51 **Keyak, J. H., Rossi, S. A., Jones, K. A., Les, C. M., and Skinner, H. B.** Prediction of fracture location in the proximal femur using finite element models. *Med. Engng Physics*, 2001, **23**, 657–664.
- 52 **Keyak, J. H. and Falkinstein, Y.** Comparison of in situ and in vitro CT scan-based finite element model predictions of proximal femoral fracture load. *Med. Engng Physics*, 2003, **25**, 781–787.
- 53 **Duncan, R. L. and Turner, C. H.** Mechanotransduction and the functional response of bone to mechanical strain. *Calcified Tissue Int.*, 1995, **57**, 344–358.

APPENDIX

Notation

E	Young's modulus (GPa)
HU	Hounsfield units of CT data
p	porosity (per cent)
t	layer thickness (mm)
w	tool path width (mm)
ρ	bone density (g/cm^3)

Subscripts

app	apparent
b	bone
c	cortical bone
s	porous scaffold material
s0	bulk scaffold material
t	trabecular bone
HA	HA scaffold material